Novel experimental methodologies to reconcile large- and small-signal responses of Hafnium-based Ferroelectric Tunnel Junctions

Novel Experimental Methodologies to Reconcile Large– and Small–Signal Responses of Hafnium–Based Ferroelectric Tunnel Junctions

Marco Massarotto[a,*], Francesco Driussi[a], Antonio Affanni[a], Suzanne Lancaster[b], Stefan Slesazeck[b], Thomas Mikolajick[b,c], David Esseni[a]

[a] *DPIA, University of Udine, Via delle Scienze 206, 33100 Udine, Italy*
[b] *NaMLab gGmbH, Nöthnitzer Str. 64a, 01187 Dresden, Germany*
[c] *IHM TU Dresden, Nöthnitzer Str. 64, 01187 Dresden, Germany*

Abstract

Ferroelectric Tunnel Junctions (FTJs) are promising electron devices which can be operated as memristors able to realize artificial synapses for neuromorphic computing. In this work, after a thorough validation of the in–house–developed experimental setup, novel methodologies are devised and employed to investigate the large– and small–signal responses of FTJs, whose discrepancies have proven difficult to interpret in previous literature. Our findings convey a significant insight into the contribution of the irreversible polarization switching to the bias–dependent differential capacitance of the ferroelectric–dielectric stack.

Keywords: Ferroelectric, Hafnium Zirconium Oxide (HZO), Ferroelectric Tunnel Junction (FTJ), Experimental Characterization, Polarization Switching, Small Signal Capacitance

*Corresponding author
Email addresses: massarotto.marco001@spes.uniud.it (Marco Massarotto), francesco.driussi@uniud.it (Francesco Driussi), antonio.affanni@uniud.it (Antonio Affanni), suzanne.lancaster@namlab.com (Suzanne Lancaster), stefan.slesazeck@namlab.com (Stefan Slesazeck), thomas.mikolajick@namlab.com (Thomas Mikolajick), david.esseni@uniud.it (David Esseni)

1. Introduction

Memory elements based on ferroelectric HfO_2 are of great interest as artificial synapses in hybrid memristive–CMOS circuits for spike–based neuromorphic computing [1–3]. In particular, Ferroelectric Tunnel Junctions (FTJs) in a Metal–Ferroelectric–Dielectric–Metal (MFDM) structure (Fig. 1) may offer high impedance and low switching energies to implement energy–efficient synaptic devices with multi–level operation [4, 5].

Nevertheless, the optimization of FTJs and other promising ferroelectric–based devices requires an in–depth analysis and experimental characterization, because of the delicate interplay between the stored polarization stability, charge trapping and the read current [6, 7]. Unfortunately, standard characterization procedures may not be sufficient to grasp the complex operation of the FTJs in its entirety. As an example, the small–signal analysis performed to evaluate the FTJs differential capacitance has led to results that are often difficult to link to the quasi–static behaviour of the ferroelectric device [8–10]. In particular, the FTJs response to AC signals shows a largely reduced contribution of the ferroelectric spontaneous polarization compared to the quasi–static characterization, which also leads to difficulties in interpreting the experimental results [8–10].

In this respect, non–standard experimental strategies may help to better understand the FTJ operation under different conditions. Here, we propose a versatile experimental setup able to characterize the FTJs both in the quasi–static regime, namely large signals at low frequency, and in the small–signal analysis, typically performed at medium/high frequency. By adjusting the parameters of our experimental setup we can measure either the current versus voltage (I–V) curves or directly the switching charge versus voltage (Q–V) characteristics of the FTJs under test. The setup has been validated both in the large–signal (hereafter referred to as LS) and in the small–signal (AC) regimes by measuring FTJs at different frequencies. Moreover, some original experimental procedures are proposed to bridge the results of LS and AC analyses.

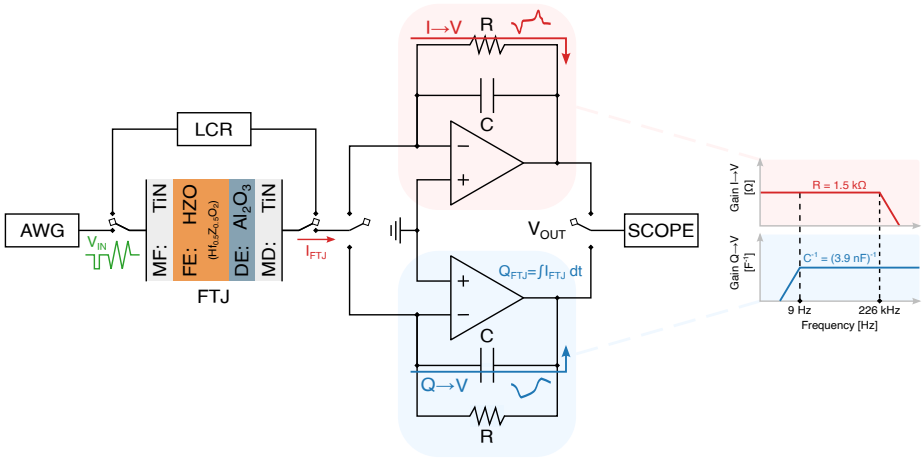

Figure 1: Sketch of the experimental setup developed for the FTJ characterization. For a given input frequency and depending on the R–C design, the virtual–grounded amplifier can operate either as an I→V converter or as a Q→V integrator to probe the switching current I_{FTJ} or charge Q_{FTJ}, respectively. The input voltage (V_{IN}) is provided by an Arbitrary Waveform Generator (AWG) and V_{OUT} is monitored over time by an oscilloscope. The transfer functions of the two configurations are sketched on the right–most side of the figure. On the left, a second setup configuration is sketched, consisting of an LCR meter directly connected to the FTJ, which we have used to compare the results of our in-house-developed converters to standard small-signal measurements.

2. Measured FTJ samples

The FTJ devices measured in this work consist of MFDM stacks fabricated by depositing 10 nm $Hf_{0.5}Zr_{0.5}O_2$ (HZO) and 2 nm Al_2O_3 via atomic layer deposition (ALD) on bottom W (30 nm)/TiN (10 nm) electrodes (see Fig. 1). To form a top contact, reactive sputtering under ultra–high vacuum is used to deposit 10 nm TiN on top. In order to stabilize the ferroelectric phase, a crystallization anneal was performed at 500 °C for 20 s. Finally, capacitors are defined by depositing Ti (10 nm) / Pt (25 nm) through a shadow mask, used as a hardmask for SC–1 etching of the TiN layer.

Table 1: Summary of the design parameters employed in this work for the I→V converter and the Q→V integrator.

CIRCUIT	R	C	RC POLE f_{RC}	CONDITION	CONVERSION	BEHAVIOR
I→V	1.5 kΩ	470 pF	226 kHz	$f_{IN} \ll f_{RC}$	$V_{OUT} = -R \times I_{FTJ}$	low–pass
Q→V	4.7 MΩ	3.9 nF	9 Hz	$f_{IN} \gg f_{RC}$	$V_{OUT} = -Q_{FTJ}/C$	high–pass

3. Design and operation of the experimental setup

As mentioned above, the investigation of the complex behaviour of the FTJs may benefit from diversified characterisation procedures able to investigate the device operation under different working conditions. For this reason, we developed the simple, low–cost and highly–versatile experimental setup sketched in Fig. 1, whose design parameters are summarized in Table 1.

The operation principle of the proposed setup is not very different from currently available commercial products [11], however, its novelty lies in the possibility to apply custom, fully–arbitrary waveforms and in the straightforward reconfiguration of the setup specifications, thus enabling an easy design of experiments intended to characterize the FTJs under test ranging from the large–signal to the small–signal regimes.

In the setup of Fig. 1, an Arbitrary Waveform Generator (AWG, Agilent 33250A) issues the driving voltage V_{IN} to the MF metal electrode of the FTJ (in this case the bottom electrode), which in turn is connected to a virtual–grounded inverting trans–impedance amplifier consisting of an OPAMP (TI TL082CP) and a feedback R–C pair. The current I_{FTJ} originating from the applied voltage flows through the amplifier feedback loop, resulting in an output voltage V_{OUT} that is finally monitored during time by an oscilloscope (Tektronix TDS520B).

Depending on the frequency f_{IN} of the driving V_{IN} signal and on the R–C feedback pole $f_{RC} = (2\pi RC)^{-1}$, the amplifier behaves either as an I→V current–to–voltage converter (for $f_{IN} \ll f_{RC}$) to measure the FTJ switching current I_{FTJ}, or as a Q→V charge–to–voltage (for $f_{IN} \gg f_{RC}$) converter that integrates I_{FTJ}, thus providing directly the switching charge Q_{FTJ}, which is linked to the switched polarization P of the ferroelectric layer of the FTJ..

The I→V and Q→V circuits share the same schematic. The reason is that the former needs a capacitor to improve the noise margin and hence the circuit stability [12], while the latter needs a resistor to provide a feedback path for the bias current of the OPAMP, which would otherwise lead to the saturation of the output node over time. Of course, the two circuits differ in the values of the lumped elements. Indeed, the R–C pair of the two distinct circuits have been chosen to allow measurements in the 10^2 – 10^5 Hz frequency range (see Table 1). Since the I→V converter has a low–pass behaviour while the Q→V integrator is a high–pass circuit, in order to measure both I_{FTJ} and Q_{FTJ} at a given frequency f_{IN} of the input signal, the bandwidths of the two circuits must overlap, as shown in the right-most sketch of Fig. 1.

4. Large–signal analysis: validation and results

The FTJ quasi–static operation is typically well described by the hysteretic polarization versus voltage (P–V) loop, which can be obtained also from the switching current versus voltage (I–V) curve. In this section, we made use of the developed setup to extract the P–V characteristics of the fabricated FTJs and investigated the dependability and the limitations of the proposed measuring schemes under the quasi–static, large–signal regime.

4.1. Optimal measurement procedure assessment

In order to probe the ferroelectric polarization switching, the FTJ is typically measured by applying triangular V_{IN} pulses. Therefore, we programmed the AWG to provide the waveform depicted in Fig. 2a: a rectangular preset pulse drives the ferroelectric HZO layer into a known initial state; then a triangular wave with a period $T = {f_{IN}}^{-1}$ is used to measure directly I_{FTJ} or Q_{FTJ}. As can be seen in Fig. 2b, the constant slope of the triangular wave allows us to visually distinguish the I_{FTJ} peaks stemming from the ferroelectric polarization switching occurring when V_{IN} crosses the FTJ coercive voltages ($\pm V_c$), from the fairly constant current plateaus due to the linear response of the dielectric stack.

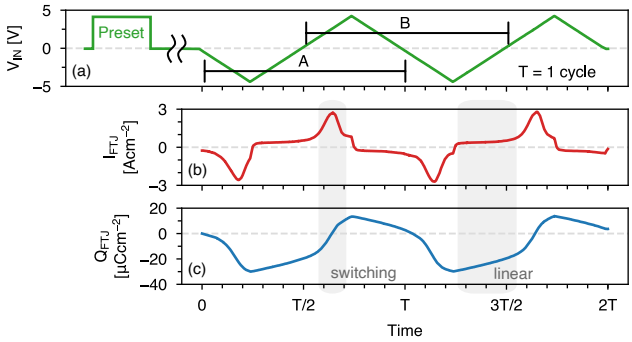

Figure 2: (a) Input voltage V_{IN} consisting of a rectangular preset pulse, followed by a triangular waveform to monitor the FTJ switching characteristics. (b) I_{FTJ} measured by the I→V converter as a function of time; the flat regions correspond to the FTJ linear dielectric response, while the peaks originate from the ferroelectric switching. (c) Switching charge Q_{FTJ} as a function of time measured by the Q→V integrator.

Moreover, Fig. 2c demonstrates how the Q→V integrator allows one to directly measure the switching charge Q_{FTJ} versus time characteristic.

Now, the I_{FTJ} and Q_{FTJ} versus time plots in Figs. 2b and 2c and the V_{IN} waveform in Fig. 2a can be combined to eliminate the time, thus obtaining the Q–V and I–V curves shown in Fig. 3. The plots in Fig. 3 allow us to extract relevant FTJ properties, such as spontaneous polarization and coercive voltages.

However, it is worth noting that, by applying a single triangular period (or equivalently considering only the first period A of the triangular pulse in Fig. 2a), the resulting I–V and Q–V characteristics may appear as the open loops shown in Fig. 3a, thus hampering the correct extraction of the FTJ properties. We attribute this issue to the high depolarization field in the ferroelectric layer which causes its partial back–switching during the delay between the preset and triangular pulses [13, 14]. At the present time, this delay cannot be properly controlled in our setup because it is due to the configuration time of the instruments. The loops distortion can be avoided by applying two subsequent triangular periods and extracting the curves from the period indicated as B in Fig. 2a, which results in the closed and un–distorted hysteretic loops shown in Fig. 3b. In the following, all reported Q–V and I–V characteristics and re-

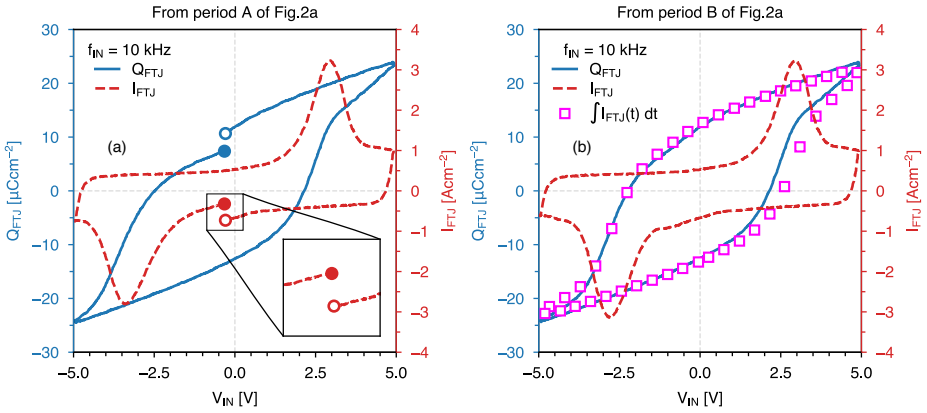

Figure 3: Q–V (blue) and I–V (red) characteristics measured by the two circuits. (a) Curves obtained from measurements in the first $[0;T]$ period (A of Fig. 2a) are distorted possibly due to the ferroelectric back–switching occurring during the delay between the preset and measurement pulses. (b) Curves obtained from measurements in the $[T/2;3T/2]$ period (B of Fig. 2a) exhibit closed hysteretic loops. The post–process integration of I_{FTJ} (magenta squares) is in excellent agreement with the direct Q_{FTJ} measurement of the Q→V integrator.

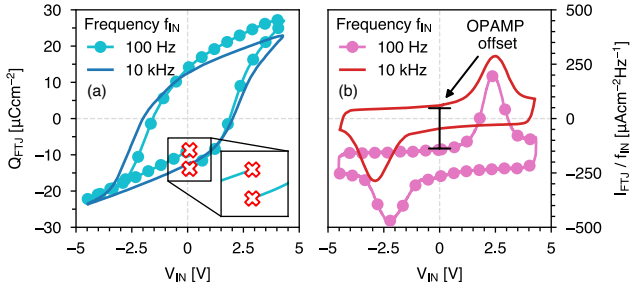

Figure 4: Frequency limitations of the two circuits. (a) Q→V integrator: for slow signals, the integration of the FTJ static leakage current tends to open the Q–V charge hysteresis loop. (b) I→V converter: the measured I_{FTJ} is proportional to the input frequency, hence at low f_{IN} the V_{OUT} becomes comparable to the OPAMP output offset, which results in a spurious shift of the curve. A post–process correction is possible in this case, provided that the OPAMP output offset is known with sufficiently high accuracy.

lated properties are obtained from data measured in the time frame indicated as period B in Fig. 2a.

4.2. Circuits equivalence and validation

The designed I→V converter and Q→V integrator directly probe I_{FTJ} and Q_{FTJ}, respectively. However, I_{FTJ} can also be converted into Q_{FTJ} through integration, while by differentiating Q_{FTJ} it is possible to obtain I_{FTJ}. Indeed, in Fig. 3b we numerically integrated the I_{FTJ} provided by the I→V converter (magenta squares) and compared it to the Q_{FTJ} measured by the Q→V integrator. The excellent agreement between the two curves demonstrates the equivalence of the two measurement schemes when f_{IN} is well inside the corresponding bandwidths. Hence, the FTJ quasi–static operation can be effectively characterized by both circuits.

However, it is worth mentioning that, depending on the specific measurement conditions, one converter may be preferred over the other because of their different frequency response (see Fig. 1). In particular, the Q→V integrator has an inherent high–pass behaviour , which may be advantageous for high–frequency characterizations. Still, possible static leakage currents through the FTJ stack are also integrated by the circuit and, especially at low frequencies when the integration time is longer, such spurious contribution can be significant enough to distort the hysteresis loop, as shown in Fig. 4a for $f_{IN} = 100$ Hz. In this case, f_{IN} is well inside the Q→V integrator bandwidth, but the tunnelling current at large V_{IN} values causes the opening of the Q–V loop [15, 16]. Indeed, the leakage current of the device under test poses a further lower–limit to the measurement frequency on top of the bandwidth of the circuits.

In this latter respect, the I→V converter is a low–pass circuit. However, it is also not suited for measurement at very low–frequencies, because of the linear proportionality between the switching current and f_{IN} [4]. In fact, at very low f_{IN}, beside the increased importance of the leakage current discussed above, the voltage $V_{OUT} = -R \times I_{FTJ}$ may become comparable to the OPAMP output offset, which can rigidly shift the measured I–V characteristic, as illustrated in

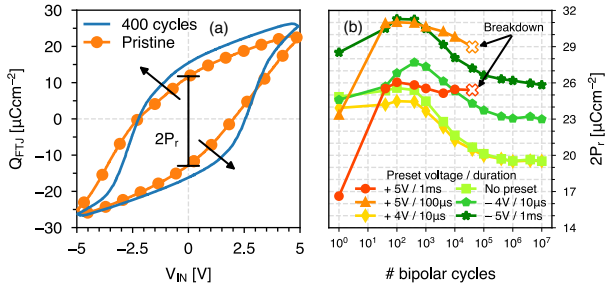

Figure 5: (a) Typical enlargement of the hysteresis loop induced by the ferroelectric wake–up, which increases $2P_r$ from the pristine (orange) to the woken–up state (blue). (b) Evolution of $2P_r$ with cycling (1 cycle = 1 period) of devices undergoing different preset pulses before each $2P_r$ measurement. The cycling pattern is the following: cycling with 100 kHz, 5 V–amplitude triangular pulses → rectangular preset pulse → $2P_r$ measurement (Fig. 2a). After the initial wake–up, ferroelectric fatigue degrades the FTJ polarization. Preset pulses boost the $2P_r$, but long positive presets may lead to early breakdown.

Fig. 4b. Fortunately, in this latter case, the offset can be compensated for in post–processing by disconnecting the FTJ and measuring the output node in zero current condition.

4.3. Preset dependent ferroelectric performance and endurance

In this section, the validated experimental setup is employed to investigate the effects of the ferroelectric wake–up and fatigue on the HZO performance. These phenomena are inherent to the ferroelectric operation and are usually attributed respectively to the redistribution and generation of defects (oxygen vacancies) in the ferroelectric layer during bipolar cycling [17]. In this work, one cycle consists of one 100 kHz triangular period with a 5 V peak amplitude.

Figure 5a demonstrates that a moderate electric field cycling favours the ferroelectric wake–up and increases the measured spontaneous polarization. In particular, the woken–up FTJ (blue, 400 cycles) exhibits a larger remnant polarization $2P_r$ and steeper switching branches compared to the not–yet–cycled pristine sample (orange). Furthermore, the wake–up effect allows us to reach a steady device operation state where the material properties can be reasonably extracted.

However, a substantially larger cycling (compared to Fig. 5a) has a detrimental effect due to ferroelectric fatigue. In this respect, Fig. 5b reports the endurance test of FTJs undergoing different rectangular preset pulses applied after each cycling sequence (consisting in n triangular pulses at 100 kHz), and before each $2P_r$ measurement (performed using the double triangular pulse illustrated in Fig. 2a). For a number of cycles larger than 10^3, all the curves show a $2P_r$ reduction.

In addition to the fatigue effect, also the preset pulse appears to affect the ferroelectric reliability. Hence, while on the one hand the preset pulses help reach higher measured $2P_r$ with respect to the no–preset case (squares), on the other hand a strong preset tends to rapidly degrade the device. Indeed, long presets with positive polarity seem to lead to an early irreversible breakdown of the devices. We attribute this phenomenon to the static leakage current through the FTJ stack, which is observed to arise asymmetrically only at large positive voltages [15, 16, 18]. For these reasons, in this work, negative and long presets have been used, in order to boost the measured polarization and at the same time preserve the FTJ integrity.

5. Small–signal analysis: validation and results

The proposed experimental setup can also be exploited to investigate the dynamic small–signal response of the FTJs, which is instead routinely investigated through LCR meters [9, 10, 19].

5.1. Conventional analysis in the AC regime

In order to test and validate the setup also for small–signal analyses, we exploited the versatility offered by the AWG to emulate the measurement sequence typically used by LCR meters for small–signal capacitance measurements.

Figure 6a sketches the issued input waveform, which consists of a $-5\,\mathrm{V}/1\,\mathrm{ms}$ negative preset pulse followed by a single period of a large–signal (LS) triangular pulse with a frequency f_{LS}, which gets interrupted by a sinusoidal (or triangular,

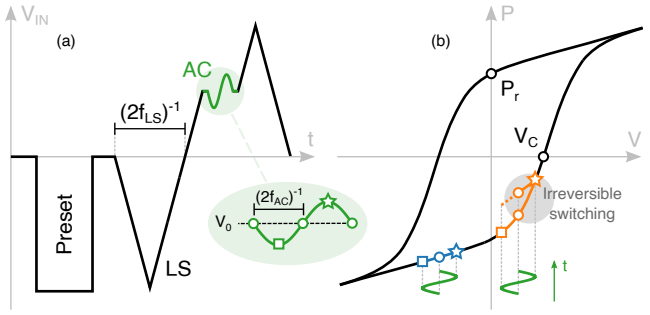

Figure 6: (a) Sketch of the waveform issued by our setup in order to mimic a small–signal measurement with an LCR meter. The quasi–static, large signal (LS) voltage is swept according to the portrayed triangular pulse. A sinusoidal (or triangular, not shown) AC signal is issued at a given V_0 bias. (b) Sketch of the minor loops followed by the FTJ under an AC stimulus when V_0 is in the linear (blue) or switching branch (orange) of the P–V curve. The complete hysteresis loop (black line) is just a guide for the eye.

not shown) AC voltage signal with a frequency f_{AC} when it reaches the desired bias V_0.

This driving signal should result in quite different I_{FTJ} depending on the V_0 value, as explained in Fig. 6b. In fact, when V_0 is far from the coercive voltage V_c (Fig. 6b, blue symbols) the I_{FTJ} response to the AC voltage signal is expected to simply reflect the linear dielectric response of the FTJ stack. Instead, for V_0 close to V_c (Fig. 6b, orange symbols), the first AC semi–period (that has the same direction of the LS variation, Fig. 6b, star symbol) is expected to induce an irreversible polarization switching (grey cloud), resulting in a non–linear component of the I_{FTJ} response to the AC voltage signal [8].

The described waveform has been applied to FTJs by using both sinusoidal (typically used in LCR meter measurements) or triangular AC signals (more suited to highlight the linear or non–linear response of the I_{FTJ}). The results are summarized in Fig. 7. For both the sinusoidal (Fig. 7a - e) and triangular (Fig. 7f - j) waveforms the I_{FTJ} response is qualitatively consistent with the behavior sketched in Fig. 6b. In fact, far from the switching edges of the P–V curve, the I_{FTJ} is a constant–amplitude sine for a sinusoidal AC stimulus (Fig. 7c), while it is a square wave for an AC triangular input (Fig. 7h). These

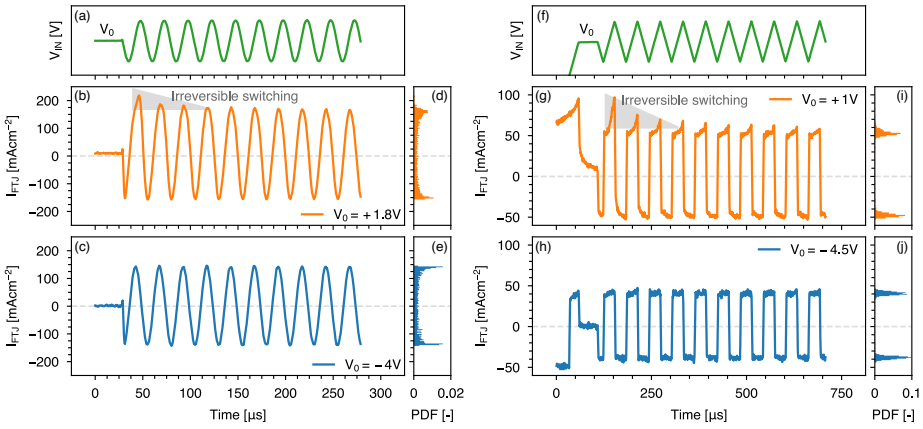

Figure 7: AC analysis with sinusoidal (a - e, f_{AC} = 40 kHz) and triangular (f - j, f_{AC} = 17 kHz) pulses. (a, f) 300 mV–amplitude AC signals are superimposed to the DC bias V_0. Reported I_{FTJ} correspond to DC biases in the switching (b, g) and linear (c, h) regions of the P–V curve (see Fig. 6b). Irreversible switching (grey triangles) is evident only in the very first issued periods and when V_0 is close to the FTJ coercive voltages ($\pm V_c$). When V_0 is far from $\pm V_c$, the I_{FTJ} amplitude is constant for all the pulses. (d, e, i, j) Probability Density Functions of I_{FTJ}, from which the I_{FTJ} amplitude can be extracted.

I_{FTJ} reveal a purely dielectric behaviour of the stack.

Instead, when V_0 is close to V_c, a non–linear behaviour of the I_{FTJ} is observed during the very first periods of the AC stimulus. For the sinusoidal AC waveform, this can be recognized in the larger positive semi–period of the I_{FTJ} response (Fig. 7b), whereas for the triangular AC it can be observed in the current peaks superimposed to the squared I_{FTJ} waveform (Fig. 7g). These additional peaks can be interpreted as a conductive component due to the charge–trapping assisting the polarization reversal [19–21].

Nevertheless, also for $V_0 \approx \pm V_c$, the quite linear response of the FTJ after the very first AC cycles seems to justify the use of the small–signal analysis (e.g. LCR meter measurements) to characterize the ferroelectric–based devices. However, the response measured by an LCR meter can hardly convey any information about the irreversible polarization switching [22].

In this respect, it is worth noting that the I_{FTJ} waveforms in Figs. 7b and 7g have larger amplitudes than the counterparts in Figs. 7c and 7h, even for the

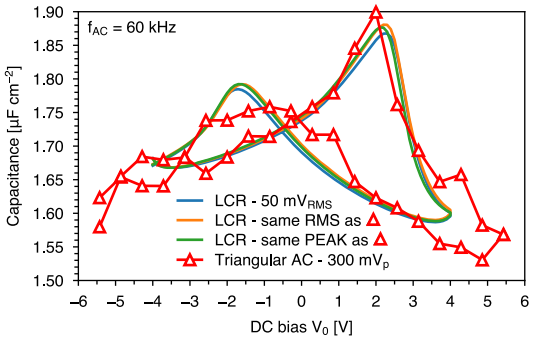

Figure 8: Comparison between the small–signal capacitance calculated from the amplitude of the I_{FTJ} originating from a 60 kHz triangular stimulus (red triangles), and those measured through an LCR meter issuing 60 kHz sinusoidal waves with 50 mV RMS value (blue), same RMS (orange) and same peak amplitude (green) as the 300 mV triangular pulses.

periods where the non-linear response has disappeared. In other words, even the linear, small–signal response is found to depend on the V_0 value.

The amplitude of the recorded waveforms has been extracted from the currents at which the maxima of the Probability Density Functions (PDF) occur. The PDFs shown in Figs. 7d, 7e, 7i and 7j have been assembled by normalizing the occurrences histogram on the bin width and the total number of measured values. Of course, this amplitude extraction method is reliable as long as the number of pulses showing switching peaks (grey–shaded areas) is small w.r.t the total number of AC pulses. However, this is not an issue for these measurements as they are meant to emulate an LCR–meter–like characterization, for which a large number of AC periods is beneficial to reduce the impact of both thermal noise and period–to–period variability.

5.2. Comparison between the developed setup and LCR meter results

In order to validate the proposed setup also in the AC regime, we compared the differential capacitance extracted from the measurements of Fig. 7 with those obtained with a conventional LCR meter (HP 4284A).

To this purpose, the triangular AC signal appears to be better suited to highlight a possible non–linear response of the FTJ. Furthermore, the PDFs

in Figs. 7i and 7j are well concentrated around their peak. Hence, at each V_0 bias, the FTJ small–signal capacitance is obtained from the results of Fig. 7 by simply dividing the amplitude of the squared I_{FTJ} (see Figs. 7g and 7h) by the slope of the triangular V_{IN} waveform. The obtained capacitance–voltage (C–V) characteristic (Fig. 8, triangles) is compared to those measured by means of the LCR meter (lines). All measurements have been performed at the same $f_{AC} =$ 60 kHz; however, to verify that the results are not dependent on the issued V_{IN} waveforms, the LCR capacitance has been measured for three different AC amplitudes: 50 mV RMS, same RMS value, and finally for the same amplitude as the 300 mV peak triangular AC waveform used in our dedicated setup.

The good agreement between all the measurement variants proves the validity of the proposed experimental setup also in the small–signal regime. Here, it is worth mentioning that, despite the simpler use of the LCR meter to extract the FTJ differential capacitance, the versatility of the setup proposed in this work enables non–standard, small–signal characterization analyses, as will be discussed in Section 6.

In order to further test the dependability of this procedure to measure the small–signal capacitance, a repeatability analysis has been performed and the results are shown in Fig. 9. In an attempt to challenge our setup and measurement procedure, we employed a 40 kHz triangular AC signal with 150 mV peak amplitude. Both the frequency and the V_{IN} peak are lower than the measurements in Fig. 8, thus resulting in smaller currents and a worse signal–to–noise ratio. Figure 9a summarizes the results of nine subsequent measurements on the same device, while Fig. 9b reports the measurement standard deviations normalized to the corresponding mean capacitance at each bias point. The low and uniform deviation values prove the good repeatability of these measurements.

6. Bridging AC analysis and LS regime

It is worth noting that the C–V curves measured with both setups (Fig. 8) show peaks corresponding to the coercive voltages, even if the contribution of

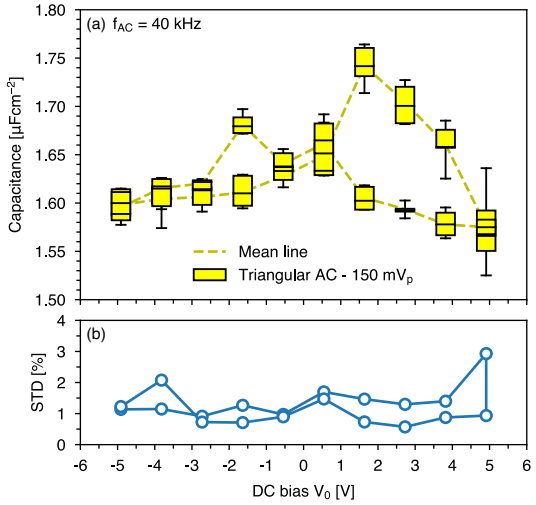

Figure 9: Repeatability analysis of the small–signal capacitance measurement employing a 40 kHz AC triangular waveform with a 150 mV peak amplitude. (a) Box–plot summarizing the results of nine subsequent measurements on the same FTJ. Markers represent the median, boxes the 25–75 percentiles and whiskers the 5–95 percentiles. (b) The standard deviation normalized to the corresponding mean capacitance value confirms good measurement repeatability.

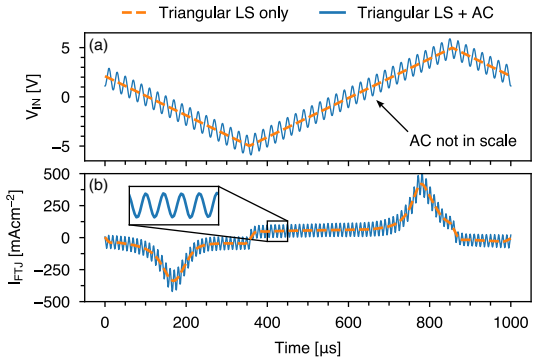

Figure 10: (a) Input signal (blue) for the fast small–signal analysis obtained as the superimposition of a slow triangular pulse (dashed orange, 1 kHz) and a 100 kHz sinusoidal waveform with a 50 mV peak amplitude. (b) The resulting I_{FTJ} (blue) shows 100 kHz sinusoidal fluctuations superimposed to the component due to the slowly varying triangular pulse (dashed orange).

irreversible switching to the PDFs in Figs. 7i and 7j is very limited. This behaviour is well known in the literature [8–10, 19, 22, 23], although a clear and convincing explanation of the magnitude of such peaks has not been provided yet. Indeed, even if the capacitance peak is commonly ascribed to the contribution of ferroelectric switching because they occur at $V_0 \approx \pm V_c$, the capacitance enhancement with respect to the minimum measured capacitance (hereafter indicated with C_{LIN}) is much smaller with respect to the peak–to–baseline ratio in the switching current measured during LS measurements (see Fig. 3). Such a quantitative difference between the results of LS analysis and C–V characterization has been proved to be difficult to interpret also in the literature, leading also to somewhat different conclusions [8–10, 19, 22–24]. In this section, we try to shed light on this disagreement by exploiting our versatile experimental setup to search for a link between the LS and AC response of FTJs.

In this respect, to simultaneously probe both AC– and LS–induced currents, the waveform sketched in Fig. 10a is issued to the FTJs. The overall waveform consists of a 100 kHz sinusoidal AC signal having a 50 mV peak amplitude superimposed to a large–signal triangular sweep whose frequency is 1 kHz and amplitude 5 V peak. The aim is to measure, at the same time, the I_{FTJ} com-

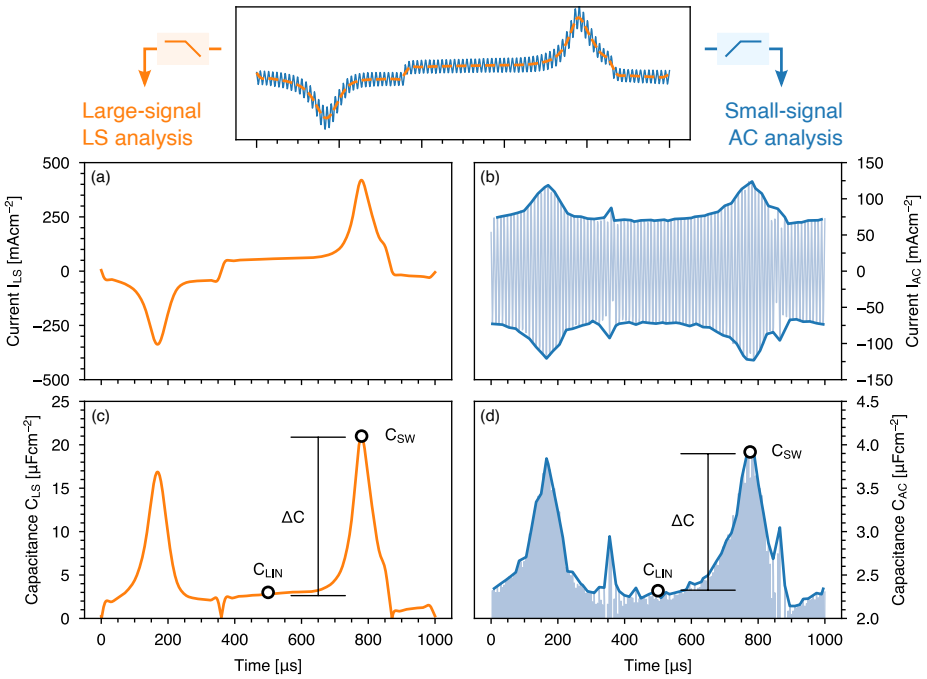

Figure 11: The components of I_{FTJ} from Fig. 10b can be separated by filtering: (a) the LS current, extracted by numerically low–pass filtering I_{FTJ}, is consistent with the measurement in Fig. 3. (b) AC current obtained by numerically high–pass filtering I_{FTJ}. (c, d) The corresponding capacitances are calculated from the LS and AC filtered current as $C_x = I_x \times (dV/dt)^{-1}$ with x = LS/AC. The linear capacitance C_{LIN}, the capacitance at the switching peak C_{SW} and their difference ΔC are indicated.

ponent due to the LS sweep and the one due to the AC signal. More precisely, we expect that the overall I_{FTJ} presents components at different frequencies reflecting both the 100 kHz sinusoidal fluctuations and the slower large–signal sweep. Indeed, the measured I_{FTJ} in Fig. 10b shows sinusoidal fluctuations superimposed to a mean value (dashed orange line) which is totally consistent with the I_{FTJ} measured with LS triangular pulses (see Fig. 3b).

We then separated the two components by numerically filtering the measured I_{FTJ}: LS and AC responses are extracted by using respectively a low–pass and a high–pass filter, with both having a cut–off frequency equal to 30 kHz. The obtained currents (I_x where x = LS/AC) are reported in Figs. 11a and 11b : the

magnitude of both I_{LS} and I_{AC} exhibit peaks for V_0 close to $\pm V_c$. We reiterate that I_{LS} in Fig. 11a is consistent with the results in Fig. 3b, thus verifying the filtering procedure.

Now, a corresponding capacitance can be calculated from these filtered I_{FTJ} components as $C_x = I_x \times (dV_x/dt)^{-1}$ with $x = LS/AC$, namely by dividing I_{LS} and I_{AC} by the derivative of the triangular sweep and of the sinusoidal waveform, respectively. Figures 11c and 11d show the obtained capacitance curves. The minimum C_{LIN} value, which is typically ascribed to the dielectric response of the stack, is quite similar in the two curves, thus indicating that, as expected, this property does not depend on the measurement regime. Instead, the capacitances C_{SW} calculated for the LS and AC regimes are different by a factor of about 7 at the C_{SW} peak. So, the difference between the capacitance peak due to the ferroelectric switching and the baseline, defined as $\Delta C = C_{SW} - C_{LIN}$, is very different between the LS and AC response of the FTJ and is consistent with the results reported in the literature [8–10, 19, 22].

After validating the dependability of our experimental procedure, in order to gain insight into this difference in the ferroelectric switching contribution to the calculated capacitance values, we varied the frequency of the LS sweep while keeping $f_{AC} = 100$ kHz. In particular, we issued signals composed of LS triangular pulses with a frequency ranging from 100 Hz to 3 kHz and monitored the relative amplitude of the C_{AC} and C_{LS} peaks, which are summarized in Fig. 12. While the C_{LS} peak is independent of the LS frequency (orange circles), the C_{AC} peak (blue squares) gradually grows with the LS frequency, lying between the LCR measurement (yellow dot–dashed line) and the LS value.

This increase of the C_{AC} peak for increasing LS frequencies reveals the importance of the speed of the LS bias. If the LS frequency is small, the FTJ undergoes a very slow V_{IN} drift, making this measurement similar to the one typically performed by the LCR meter, namely at a constant V_0 bias with an AC signal superimposed (see Fig. 7a). So, the C_{AC} peak approaches the LCR meter measurement (Fig. 12, yellow dot–dashed line) at low LS frequency.

Instead, when the LS frequency is larger, apparently the ferroelectric switch-

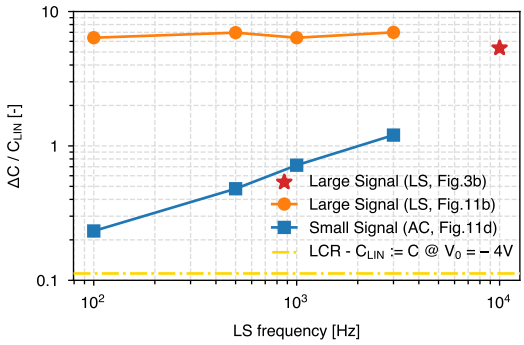

Figure 12: Relative difference between C_{SW} and C_{LIN} obtained from the analysis as in Fig. 11. Orange circles: the switching capacitance peak induced by the slow LS sweep (see Fig. 11b) is independent of the triangular pulse frequency. Blue squares: the AC capacitance, obtained as in Fig. 11d, exhibits a peak that decreases at smaller LS frequencies, converging towards the result obtained with the LCR meter (yellow dot–dashed line) due to the smaller contribution of the irreversible switching to the extracted capacitance.

ing contributes much more to C_{AC}, leading to higher peaks similar to those measured during the LS characterization. This can be due to the fact that ferroelectric switching does not have enough time to be completed during the V_{IN} drift imposed by the LS sweep, so it largely contributes also to the AC response, leading to higher peaks in the calculated C_{AC} that approach those observed in the analysis of the LS response.

It is evident that the measurements in Fig. 12 represent an experimental procedure that closes the gap between the LS characterization and the AC analysis of the FTJs.

7. Conclusions

We here described a dedicated experimental setup and new measurement procedures that go beyond the conventional FTJ characterizations. Such characterization techniques have been first validated both in the large–signal (LS) and small–signal (AC) regimes and then applied to fabricated FTJ devices, aiming to highlight characteristic features of the given dielectric stack.

First, our versatile setup is able to operate either as an I→V converter or as a Q→V integrator, to respectively measure the FTJ switching current or directly the switching charge. The different bandwidths of the two circuits offer distinct advantages based on the explored frequency range. In particular, at high frequencies, the proposed Q→V integrator (high–pass response) can outperform the more conventional I→V converter (low–pass behavior).

The measurement of the P–V characteristics showed the impact of cycling, which first enhances the ferroelectric performance thanks to the wake–up of the devices, and then eventually degrades the FTJ reliability due to the ferroelectric fatigue. In both cases, the proper selection of the preset pulse before the $2P_r$ measurements may improve the FTJ characteristics and preserve the devices from an early breakdown.

We also investigated the FTJs in the small–signal regime, demonstrating that the use of standard LCR meters is justified to probe the differential capacitance, since our measurements evidenced contributions from the irreversible polarization switching only in the very first periods of the AC signal, and then showed decent linearity in response to the following AC cycles.

Finally, we proposed a novel characterization method that allowed us to measure both the large– and small–signal responses of FTJs within a single measurement. This new technique goes beyond the conventional LS and AC characterization methods, in that the electrical stimulus can trigger the polarization switching and, at the same time, the response to an AC signal, which in this case displays a clear contribution from the irreversible switching. In particular, we have shown that the speed of the background bias plays a crucial role in the measured values of the AC capacitance. In fact, the faster the bias is, the closer the measured AC capacitance is to the corresponding LS capacitance. In this respect, we here reported, for the first time to our knowledge, results that create a bridge between small-signal and large–signal experiments on FTJs. Therefore, we consider this technique a new and very valuable tool to gain a better insight into the ferroelectric polarization switching and the charge–trapping behaviour.

Acknowledgment

This work was supported by the European Union through the BeFerroSynaptic project (GA:871737).

References

[1] S. Slesazeck, V. Havel, E. Breyer, H. Mulaosmanovic, M. Hoffmann, B. Max, S. Duenkel, T. Mikolajick, Uniting The Trinity of Ferroelectric HfO2 Memory Devices in a Single Memory Cell, in: 2019 IEEE 11th International Memory Workshop (IMW), 2019, pp. 1–4. doi:10.1109/IMW.2019.8739742.

[2] S. Yu, Neuro-inspired computing with emerging nonvolatile memories, Proceedings of the IEEE 106 (2) (2018) 260–285. doi:10.1109/JPROC.2018.2790840.

[3] S. Slesazeck, T. Mikolajick, Nanoscale resistive switching memory devices: A review, Nanotechnology 30 (35) (2019) 352003. doi:10.1088/1361-6528/ab2084.

[4] E. Covi, Q. T. Duong, S. Lancaster, V. Havel, J. Coignus, J. Barbot, O. Richter, P. Klein, E. Chicca, L. Grenouillet, A. Dimoulas, T. Mikolajick, S. Slesazeck, Ferroelectric Tunneling Junctions for Edge Computing, in: 2021 IEEE International Symposium on Circuits and Systems (ISCAS), 2021, pp. 1–5. doi:10.1109/ISCAS51556.2021.9401800.

[5] R. Fontanini, M. Segatto, K. S. Nair, M. Holzer, F. Driussi, I. Häusler, C. T. Koch, C. Dubourdieu, V. Deshpande, D. Esseni, Charge-Trapping-Induced Compensation of the Ferroelectric Polarization in FTJs: Optimal Conditions for a Synaptic Device Operation, IEEE Transactions on Electron Devices 69 (7) (2022) 3694–3699. doi:10.1109/TED.2022.3175684.

[6] B. Max, M. Hoffmann, S. Slesazeck, T. Mikolajick, Direct correlation of ferroelectric properties and memory characteristics in ferroelectric tunnel

junctions, IEEE Journal of the Electron Devices Society 7 (2019) 1175–1181. doi:10.1109/JEDS.2019.2932138.

[7] R. Fontanini, M. Segatto, M. Massarotto, R. Specogna, F. Driussi, M. Loghi, D. Esseni, Modeling and design of FTJs as multi-level low energy memristors for neuromorphic computing, IEEE Journal of the Electron Devices Society 9 (2021) 1202–1209. doi:10.1109/JEDS.2021.3120200.

[8] K. Toprasertpong, M. Takenaka, S. Takagi, Direct observation of interface charge behaviors in fefet by quasi-static split c-v and hall techniques: Revealing fefet operation, in: 2019 IEEE International Electron Devices Meeting (IEDM), 2019, pp. 23.7.1–23.7.4. doi:10.1109/IEDM19573.2019.8993664.

[9] J. Li, Y. Qu, M. Si, X. Lyu, P. D. Ye, Multi-probe characterization of ferroelectric/dielectric interface by c-v, p-v and conductance methods, in: 2020 IEEE Symposium on VLSI Technology, 2020, pp. 1–2. doi:10.1109/VLSITechnology18217.2020.9265069.

[10] Y. Qu, J. Li, M. Si, X. Lyu, P. D. Ye, Quantitative characterization of interface traps in ferroelectric/dielectric stack using conductance method, IEEE Transactions on Electron Devices 67 (12) (2020) 5315–5321. doi:10.1109/TED.2020.3034564.

[11] Radiant Technologies Inc., Premier II Ferroelectric Tester, https://www.ferrodevices.com/precision-non-linear-materials-testers/premier-ll-ferroelectric-tester/, [Online, accessed 2022-July-28].

[12] Texas Instruments Inc., Compensate transimpedance amplifiers intuitively, Tech. rep., [Online, accessed 2022-July-28].

[13] S. Lancaster, P. D. Lomenzo, M. Engl, B. Xu, T. Mikolajick, U. Schroeder, S. Slesazeck, Investigating charge trapping in ferroelectric thin films through transient measurements, Frontiers in Nanotechnology 4 (2022) , pp. 1–11. doi:10.3389/fnano.2022.939822.

[14] B. Max, T. Mikolajick, M. Hoffmann, S. Slesazeck, T. Mikolajick, Retention Characteristics of Hf0.5Zr0.5O2-Based Ferroelectric Tunnel Junctions, in: 2019 IEEE 11th International Memory Workshop (IMW), 2019, pp. 1–4. doi:10.1109/IMW.2019.8739765.

[15] M. Massarotto, F. Driussi, A. Affanni, S. Lancaster, S. Slesazeck, T. Mikolajick, D. Esseni, Versatile experimental setup for FTJ characterization, Solid-State Electronics 194 (2022) 108364. doi:https://doi.org/10.1016/j.sse.2022.108364.

[16] M. Yamaguchi, S. Fujii, Y. Kamimuta, S. Kabuyanagi, T. Ino, Y. Nakasaki, R. Takaishi, R. Ichihara, M. Saitoh, Impact of specific failure mechanisms on endurance improvement for HfO2-based ferroelectric tunnel junction memory, IEEE 2018 International Reliability Physics Symposium 2018-March (2) (2018) 6D.21–6D.26. doi:10.1109/IRPS.2018.8353633.

[17] M. Pešić, F. P. G. Fengler, L. Larcher, A. Padovani, T. Schenk, E. D. Grimley, et al., Physical mechanisms behind the field-cycling behavior of HfO2-based ferroelectric capacitors, Advanced Functional Materials 26 (25) (2016) 4601–4612. doi:10.1002/adfm.201600590.

[18] J. F. Verweij, J. H. Klootwijk, Dielectric breakdown I: A review of oxide breakdown, Microelectronics Journal 27 (7) (1996) 611–622. doi:10.1016/0026-2692(95)00104-2.

[19] M. Si, X. Lyu, P. D. Ye, Ferroelectric Polarization Switching of Hafnium Zirconium Oxide in a Ferroelectric/Dielectric Stack, ACS Applied Electronic Materials 1 (5) (2019) 745–751. doi:10.1021/acsaelm.9b00092.

[20] J. Li, M. Si, Y. Qu, X. Lyu, P. D. Ye, Quantitative Characterization of Ferroelectric/Dielectric Interface Traps by Pulse Measurements, IEEE Transactions on Electron Devices 68 (3) (2021) 1214–1220. doi:10.1109/TED.2021.3053497.

[21] H. W. Park, S. D. Hyun, I. S. Lee, S. H. Lee, Y. B. Lee, M. Oh, B. Y. Kim, S. G. Ryoo, C. S. Hwang, Polarizing and depolarizing charge injection through a thin dielectric layer in a ferroelectric–dielectric bilayer, Nanoscale 13 (2021) 2556–2572. doi:10.1039/D0NR07597C.

[22] M. Segatto, M. Massarotto, S. Lancaster, Q. T. Duong, A. Affanni, R. Fontanini, F. Driussi, D. Lizzit, T. Mikolajick, S. Slesazeck, D. Esseni, Polarization switching and AC small-signal capacitance in Ferroelectric Tunnel Junctions, in: IEEE 52nd European Solid-State Device Research Conference (ESSDERC), 2022, pp. 340–343. doi:10.1109/ESSDERC55479.2022.9947185.

[23] H. Li, G. Subramanyam, Capacitance of thin-film ferroelectrics under different drive signals, IEEE Transactions on Ultrasonics, Ferroelectrics, and Frequency Control 56 (9) (2009) 1861–1867. doi:10.1109/TUFFC.2009.1262.

[24] D. Bolten, U. Böttger, R. Waser, Reversible and irreversible polarization processes in ferroelectric ceramics and thin films, Journal of Applied Physics 93 (3) (2003) 1735–1742. doi:10.1063/1.1535748.